J. Fluid Mech. (2025), *vol.* 1017, A8, doi:10.1017/jfm.2025.10480

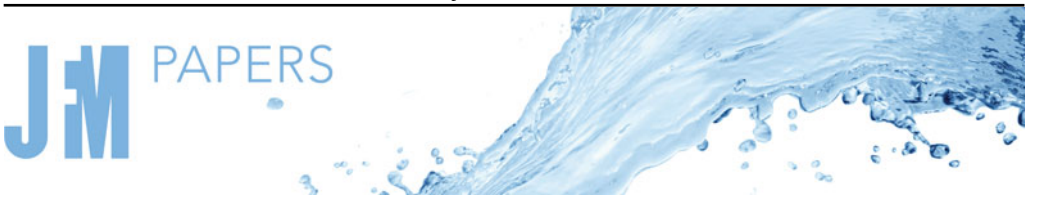

Linear reactive control of jet installation noise

Matteo Mancinelli[1], **Diego Bonkowski de la Sierra Audiffred**[2], **Eduardo Martini Rodrigues da Silva**[3], **Peter Jordan**[3], **André Cavalieri**[2] and **Anton Lebedev**[3]

[1]Department of Civil Engineering, Computer Science and Aeronautical Technologies, Università Roma Tre, Via Vito Volterra 62, 00146 Rome, Italy

[2]Department of Aeronautical Engineering, Instituto Tecnológico de Aeronáutica, São José dos Campos, Brazil

[3]Department of Fluids, Thermal Science and Combustion, Institut Pprime, CNRS-Université de Poitiers-ENSMA, 11 Boulevard Marie et Pierre Curie, 86360 Chasseneuil-du-Poitou, France

Corresponding author: Matteo Mancinelli, matteo.mancinelli@uniroma3.it

(Received 27 November 2024; revised 26 May 2025; accepted 14 July 2025)

This paper presents an experimental application of reactive control to jet installation noise based on destructive interference. The work is motivated by the success of previous studies in applying this control approach to mixing layers (Sasaki *et al.* Theor. 2018*b* *Comput. Fluid Dyn*. **32**, 765–788), boundary layers (Brito *et al.* 2021 *Exp. Fluids* **62**, 1–13; Audiffred *et al.* 2023 *Phys. Rev. Fluids* **8**, 073902), flow over a backward-facing step (Martini *et al.* 2022 *J. Fluid Mech*. **937**, A19) and, more recently, to turbulent jets (Maia *et al.* 2021 *Phys. Rev. Fluids* **6**, 123901; Maia *et al.* 2022 *Phys. Rev. Fluids* **7**, 033903; Audiffred *et al.* 2024b J. *Fluid Mech*. **994**, A15). We exploit the fact that jet–surface interaction noise is underpinned by wavepackets that can be modelled in a linear framework and develop a linear control strategy where piezoelectric actuators situated at the edge of a scattering surface are driven in real time by sensor measurements in the near field of the jet, the objective being to reduce noise radiated in the acoustic field. The control mechanism involves imposition of an anti-dipole at the trailing edge to cancel the scattering dipole that arises due to an incident wavepacket perturbation. We explore two different control strategies: (i) the inverse feed-forward approach, where causality is imposed by truncating the control kernel, and (ii) the Wiener–Hopf approach, where causality is optimally enforced in building the control kernel. We show that the Wiener–Hopf approach has better performance than that obtained using the truncated inverse feed-forward kernel. We also explore different positions of the near-field sensors and show that control performance is better for sensors installed for streamwise positions downstream in the jet plume, where the signature of hydrodynamic wavepacket is better captured by the sensors. Broadband noise reductions of up to 50 % are achieved.

Key words: jet noise, noise control, aeroacoustics

1. Introduction

The turbulent jet exhausting from an aircraft engine is one of the main sources of aircraft noise, especially during take off, when engines run at maximum power. This issue imposes constraints on the development of commercial aircraft. In addition to the technological and sustainability aspects, jet noise remains a challenging scientific problem because most of the fluctuation energy in subsonic turbulent jets is not converted into sound energy: jets are populated by mostly silent flow structures. There is now consensus that coherent structures, referred to also as wavepackets, are the most acoustically efficient structures (Cavalieri *et al.* 2011, 2012; Cavalieri & Agarwal 2014; Sinha *et al.* 2014). These structures, which are largely underpinned by Kelvin–Helmholtz and Orr instability mechanisms, can be described by linear models (Jordan & Colonius 2013; Cavalieri, Jordan & Lesshafft 2019).

The installation of a jet in the vicinity of a scattering surface, such as a wing, generates an additional noise source referred to in the literature as jet–surface interaction (JSI) noise (Brown 2013). As shown by Cavalieri *et al.* (2014), Piantanida *et al.* (2016), Nogueira, Cavalieri & Jordan (2017) and Nogueira *et al.* (2019), the physical mechanism underlying generation of JSI noise is the scattering of coherent structures by the trailing edge (TE) of the surface. In these studies, the authors show, using acoustic-analogy-based models, the effectiveness of linear models for the JSI noise problem. The utility of linearised approaches for the phenomenon was also shown by Faranosov *et al.* (2019), who used a Wiener–Hopf estimator to predict far-field noise on the basis of near-field pressure fluctuations provided by parabolised stability equations. The fact that JSI noise is underpinned by wavepackets and amenable to modelling in a linear framework, suggests that a linear reactive flow-control strategy that targets coherent structures could be used to reduce JSI noise.

Reactive control is a strategy where the actuation signal is driven in real time on the basis of flow measurements. In this framework, linear quadratic Gaussian (LQG) controllers have been widely adopted for flow control to design optimal control tools, e.g. for separated boundary layers (Åkervik *et al.* 2007), flows over an open cavity (Barbagallo, Sipp & Schmid 2009) and a backward-facing step (Barbagallo *et al.* 2012). The drawback of LQG controllers is that their implementation requires the solution of two algebraic Riccati equations for the estimation of the system state and the control-kernel calculation. Due to the high dimensionality of fluid systems, the use of a reduced-order model is required. Reduced-order models may be obtained using, for instance, either balanced Proper Orthogonal Decomposition truncation (Bagheri *et al.* 2009) or linear stability theory (Sasaki *et al.* 2017). An alternative, simpler approach for flow systems underpinned by convective instability mechanisms involves the elimination of disturbances via a destructive superposition of waves: wave cancellation. This strategy has recently been used, for instance, for the control of free shear flow (Sasaki *et al.* 2018*b*) and a boundary layer (Sasaki *et al.* 2018*a*), where it also gave evidence of comparable performances with respect to the more computationally demanding LQG controller. Wave-cancelling approaches have the further advantage that they are based on transfer functions (TFs) that can be educed from experiments in a system-identification approach, as shown by Brito *et al.* (2021) and Audiffred *et al.* (2023) for the control of Tollmien–Schlichting waves. Concerning jets, wave-cancellation schemes were applied to control: (i) harmonic disturbances in free jets using an open-loop strategy (Kopiev *et al.* 2013); (ii) stochastic

disturbances in forced and unforced laminar and turbulent free jets (Maia *et al.* 2021, 2022; Audiffred *et al.* 2024*b*); harmonic disturbances in excited and unexcited installed jets (Bychkov *et al.* 2019; Kopiev *et al.* 2020). With reference to the last work, plasma actuators at the nozzle exit were driven by near-field sensors via a feedback control scheme to reduce the wavepacket amplitude, thus reducing the noise scattered by the TE of the surface.

The above discussion motivates the present work, where we perform linear reactive control of JSI noise for an unexcited subsonic jet over a broadband frequency range. We design an experiment comprising a subsonic turbulent jet in the vicinity of a parallel flat plate to mimic jet–wing interaction. Pressure sensors in the near field of the jet are used to drive downstream actuators installed on the TE of the surface to reduce the noise radiated in the acoustic field. The potentialities of this set-up to effectively control jet installation noise have been explored in the model designed by Karban, Martini & Jordan (2024), where the jet dynamics was represented by a stochastic wavepacket modelled using the Ginzburg–Landau equation and the actuation was mimicked by a point dipole placed at the TE of a semi-infinite flat plate. The near-field sensors and the acoustic observer consist, respectively, of a 6-microphone azimuthal array to measure the axisymmetric pressure disturbances and two microphones located in the sound field on the shielded and unshielded sides of the jet–plate system. Transfer functions between sensors, observers and actuators used to build the control kernel are directly obtained from the experiments. Consistent with the results of Mancinelli, Jordan & Lebedev (2024), where the sensor–observer coherence was shown to vary strongly with the streamwise position of the near-field sensors, we explore control for two axial positions of the near-field sensor array where the sensor–observer coherence showed high amplitude, that is, at the nozzle exhaust and in the vicinity of the TE. Two control strategies are tested: (i) the inverse feed-forward control (IFFC) (Sasaki *et al.* 2018*a*; Brito *et al.* 2021) and (ii) the Wiener–Hopf (W–H) control (Noble & Weiss 1959; Martini *et al.* 2022). Consistent with the results obtained by Audiffred *et al.* (2023) and Audiffred *et al.* (2024*b*) for the control of Tollmien–Schlichting waves in a boundary layer over a wing profile and the velocity fluctuations in a turbulent jet, respectively, we show that the W–H formalism yields to a better performance than that achieved using the IFFC approach.

The remainder of the paper is organised as follows. Section 2 provides the theoretical framework of linear reactive control, § 3 describes the experimental set-up and § 4 is devoted to the presentation of the main results. Conclusions and future developments of the present activity are finally discussed in § 5.

2. Linear reactive control

The principle of linear reactive control for installed jet noise consists of using actuators installed at the TE of the surface to generate an anti-dipole that would cancel the scattering dipole that arises due to an incident perturbation field associated with convecting wavepackets. A simplified sketch of the control strategy just outlined is shown in figure 1, where we use lower- and upper-case symbols to denote time- and frequency-domain quantities, respectively.

The actuation signal in the frequency domain is (Brito *et al.* 2021)

$$U(f) = K(f)\Upsilon(f), \tag{2.1}$$

where U is the actuation signal, Υ is the sensor reading and K is the control kernel. In the time domain, the actuation signal u is given by the convolution

$$u\,(t) = \int_{-\infty}^{+\infty} k\,(\tau)\,\upsilon\,(t-\tau)\;\mathrm{d}\tau, \tag{2.2}$$

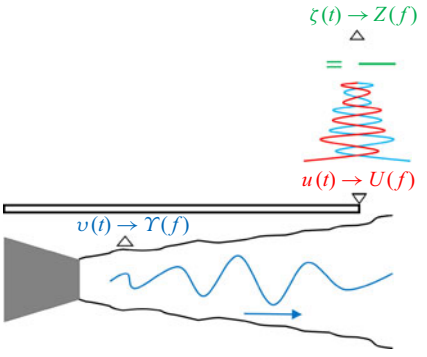

Figure 1. Schematic representation of the feed-forward wave-cancellation strategy for the JSI noise control. Here, υ (Υ) denotes the near-field sensor, u (U) the actuator and ζ (Z) the observer in the acoustic field. Lower-case symbols denote quantities in the time domain, upper-case symbols denote their counterparts in the frequency domain.

leading to a solution where, in general, the actuation signal is non-causal, that is, it depends on negative values of τ. In real applications this is not feasible, given that the actuation would depend on sensor readings in the future. For the control to be causal

$$k\,(\tau < 0) = 0, \tag{2.3}$$

needs to be imposed. We address this causality issue using two approaches: (i) the IFFC, where causality is imposed by the truncation of the control kernel to positive τ, and (ii) the W–H control, where causality is imposed *a priori*.

2.1. *Inverse feed-forward control*

The control law design is based on that presented by Sasaki *et al.* (2018*a*) and Maia *et al.* (2021) and the corresponding block diagram is shown in figure 2. We seek to eliminate fluctuations at the observer ζ, which in the frequency domain are given by

$$Z(f) = \Upsilon(f) H_{\upsilon\zeta}(f) + U(f) H_{u\zeta}(f), \tag{2.4}$$

where $H_{\upsilon\zeta}$ and $H_{u\zeta}$ are the sensor–observer and actuator–observer TFs, respectively. The actuation can be written as follows:

$$U(f) = K(f)\,(\Upsilon(f) + H_{u\upsilon}(f) U(f)), \tag{2.5}$$

where $H_{u\upsilon}$ is the actuator–sensor TF, accounting for potential contaminations of the sensor measurements by the actuators and $\Upsilon(f)$ is, consequently, the uncontaminated sensor reading. As pointed out by Maia *et al.* (2021), this should not be confused with a classic feedback configuration, where actuation is modified by a downstream sensor, and use of the contamination TF is exploited to avoid undesirable noise in the actuation signal. Combining (2.4) and (2.5) and setting $Z(f) = 0$, we find the control kernel

$$K(f) = -\frac{H_{\upsilon\zeta}}{H_{u\zeta} - H_{u\upsilon} H_{\upsilon\zeta}}. \tag{2.6}$$

To regularise the problem and avoid divisions by zero (or values close to zero), (2.6) is recast as

$$K(f) = -\frac{\left(H_{u\zeta} - H_{u\upsilon} H_{\upsilon\zeta}\right)^{*} H_{\upsilon\zeta}}{\left(H_{u\zeta} - H_{u\upsilon} H_{\upsilon\zeta}\right)^{*} \left(H_{u\zeta} - H_{u\upsilon} H_{\upsilon\zeta}\right) + R}, \tag{2.7}$$

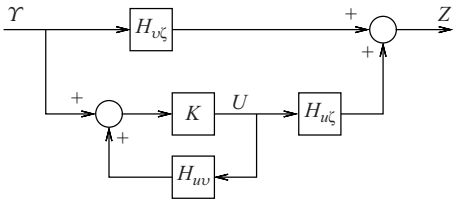

Figure 2. Block diagram of the control scheme implemented herein.

where the superscript * denotes the complex conjugate and R is a penalisation factor typically frequency dependent, analogous to the actuator penalty in the LQG and W–H frameworks (see § 2.2). In this work we consider R as a constant in the frequency domain, that is, corresponding to a white noise signal in time, and explore different values with a view to maximising the control performance. The control law in the time domain is,

$$u\,(t) = \int_0^\infty k\,(\tau)\,\upsilon\,(t-\tau)\;\mathrm{d}\tau, \tag{2.8}$$

where the control kernel is truncated to positive τ to impose the causality constraint *a posteriori*. The TFs are obtained from the experiments and estimated as the ratio between the cross-spectral densities (*CSD*) of inputs and outputs and the power spectral densities of inputs (Bendat & Piersol 2011)

$$H_{\upsilon\zeta} = \frac{S_{\upsilon\zeta}}{S_{\upsilon\upsilon}}, \tag{2.9a}$$

$$H_{u\zeta} = \frac{S_{u\zeta}}{S_{uu}}, \tag{2.9b}$$

$$H_{u\upsilon} = \frac{S_{u\upsilon}}{S_{uu}}, \tag{2.9c}$$

where $S_{\upsilon\zeta}$ is the sensor–observer *CSD*, $S_{u\zeta}$ is the actuator–observer *CSD*, $S_{u\upsilon}$ is the actuator–sensor *CSD* and $S_{\upsilon\upsilon}$ and S_{uu} are the sensor and actuator signal auto-spectra, respectively. Spectral densities are estimated using Welch's method (Welch 1967), using a Hanning window of 1024 samples with a total length of 60 s and a sampling frequency of 10 kHz, thus leading to a frequency resolution of $\approx$10 Hz, and 50 % overlap.

2.2. *Wiener–Hopf control*

The W–H control results in an optimal control where a quadratic cost functional is minimised. The cost functional is given by

$$J = \int_{-\infty}^{+\infty} \left(\left\langle \zeta_c^* Q \zeta_c + u_+^* R u_+ \right\rangle + k_+\lambda_- + k_+^*\lambda_-^*\right)\,\mathrm{d}t, \tag{2.10}$$

where ζ_c is the controlled observer signal, λ_- is a Lagrange multiplier, where $\lambda_-(t > 0) = 0$ to impose causality, that is, $k_+(t < 0) = 0$, $\langle\cdot\rangle$ denotes an ensemble average, Q is a weighting parameter of state deviation from original condition and R a control penalisation of the same kind described above (cf. (2.7)). From (2.10), the functional is, up to a multiplicative constant, a function of R/Q. We thus use, without loss of generality, $Q = 1$. The subscripts $+$ and $-$ imply that the associated functions are regular in the upper and lower half-planes of the complex frequency plane, respectively, such that plus and minus functions are zero for $t < 0$ and $t > 0$, respectively, when transformed to the time domain.

Recalling that, according to (2.2), $u = k * \upsilon$, where $*$ denotes a convolution, the controlled signal can be expressed as a linear combination of the uncontrolled signal ζ_{unc} and the actuation response, as formalised in what follows

$$\zeta_c = \zeta_{unc} + h_{u\zeta} * u = \zeta_{unc} + h_{u\zeta} * k * \upsilon, \tag{2.11}$$

where $h_{u\zeta}$ is the actuation–observer TF in the time domain. The minimisation of the functional in (2.10) leads to the following W–H equation in the frequency domain (for more details on the solution of the W–H problem see Appendix A):

$$H_l K_+ S_{\upsilon\upsilon} + \lambda^*_- = H_r S_{\upsilon\zeta}, \tag{2.12}$$

where H_l and H_r are defined as follows:

$$H_l(f) = H^*_{u\zeta}(f) Q H_{u\zeta}(f) + R, \tag{2.13a}$$

$$H_r(f) = -H^*_{u\zeta}(f) Q. \tag{2.13b}$$

Applying the additive and multiplicative factorisations described in Appendix A, the following expression for the control kernel is obtained:

$$K_+ = H^{-1}_{l_+} \left(H^{-1}_{l_-} H_r S_{\upsilon\zeta} S^{-1}_{\upsilon\upsilon_-} \right)_+ S^{-1}_{\upsilon\upsilon_+}, \tag{2.14}$$

where the frequency dependence was omitted for notational simplicity. To account for the feedback effect, that is, the influence of the actuator u on the sensor υ, the final expression for the control kernel is (Martini *et al.* 2022)

$$K'_+(f) = (I + K_+ H_{u\upsilon})^{-1} K_+, \tag{2.15}$$

which is then inverse-Fourier transformed to obtain a causal control kernel in the time domain.

3. Experimental set-up

Experiments were performed in the Bruit & Vent anechoic facility of Institut Pprime in Poitiers. The anechoic chamber is $12.6 \times 10.6 \times 7.85\,\mathrm{m}^3$ in size and is equipped with absorbing acoustic foam leading to a cutoff frequency of 200 Hz. The feed line consists of a compressed dry-air duct supplied by a screw compressor delivering a continuous mass flow rate of up to $1\,\mathrm{kg\,s}^{-1}$ at 3.5 bar. An electrically driven valve downstream of the compressor allows regulation of the jet velocity by controlling the incoming mass flow. A cooling system is installed downstream of the regulating valve to provide a jet flow in isothermal conditions with respect to the ambient temperature. The stagnation temperature and pressure in the plenum chamber are monitored through a thermocouple and a pressure transducer, respectively. The jet issues from a straight nozzle of diameter $D = 0.05$ m. The boundary layer inside the nozzle is tripped by a strip of carborundum particles placed 2.5 diameters upstream of the nozzle exit so as to generate an initially turbulent jet. The same flow, i.e. nozzle geometry and boundary-layer trip, was studied in several previous works (see e.g. Cavalieri *et al.* 2013; Jaunet, Jordan & Cavalieri 2017; Maia, Jordan & Cavalieri 2022; Audiffred *et al.* 2024*a*).

A steel flat plate is installed parallel to the jet at the radial distance $H = 1D$ from the nozzle axis with the TE positioned at an axial distance $x/D = 2$ from the nozzle exhaust. The piezoelectric actuators are P876.A11 DuraAct Patch transducers and are driven by a E-413.D2 DuraAct amplifier. They are installed at the TE of the plate and their streamwise length, spanwise width and thickness are equal to 0.8 D, 0.7 D and 0.008 D, respectively. For the results reported here, the five central actuation patches alone were used to control,

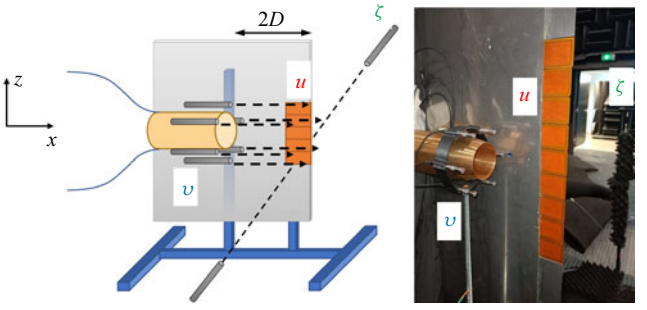

Figure 3. Sketch and picture of the experimental set-up and microphone disposition and identification of the reference system adopted.

as this is where the jet-edge dipole is centred. We use a near-field microphone array as sensors. The 6-microphone azimuthal array is placed at a radial distance of $r = 0.9\,D$ from the nozzle axis to measure the pressure fluctuations in the near field and to extract the azimuthal Fourier mode $m = 0$, which is the most efficient mode in the generation of installed jet noise (Cavalieri *et al.* 2014). The near-field array can be moved along the streamwise direction. Consistent with the results presented by Mancinelli *et al.* (2024), where the sensor–observer TF was characterised in the same experimental set-up with the aim of providing guidance for sensor positioning for control, we consider two different streamwise positions of the array, $x/D = 0$ and $x/D = 1.7$. Two microphones are placed in the acoustic field at the TE axial position at a radial distance of 13 D from the TE. The microphone observers are installed at polar angles $\psi = 90°$ and $\psi = 270°$, where the polar angle ψ is positive in the downstream direction, on the shielded and scattered sides of the acoustic field, respectively, where the dipole TE noise source has peak radiation. We mostly focus on control results obtained using the microphone on the shielded side as observer position. The shielded side has two advantages: the direct jet noise, which we do not attempt to control, contributes less; the scattered sound does not radiate through the jet, minimising complications associated with flow–sound interaction (refraction, scattering by turbulence). Control results obtained on the unshielded side are addressed in Appendix B.

Measurements are carried out in isothermal conditions for jet Mach numbers $M = 0.2$, 0.25 and 0.3, which correspond to nozzle-diameter-based Reynolds numbers, Re, of 2.2×10^5, 2.8×10^5 and 3.4×10^5, respectively. Low-velocity conditions are dictated by limitations of the actuation system. Pressure fluctuations are measured by PCB 46BP microphones, whose frequency response is flat in the range 4 Hz–70 kHz. Sensor and observer readings and actuation are performed using a DSPACE MicroLabBox DS1202 Controller Board. The controller ran at a sampling rate, f_s, of 10 kHz for an acquisition time $T_a = 60$ s on the basis of a Simulink plant model that was converted to the dSPACE Control Desk environment. A sketch and a picture of the experimental set-up and the microphone disposition with the identification of the reference system adopted are shown in figure 3.

4. Results

4.1. *Actuation characterisation*

We characterise the actuator response to identify the operational frequency range and explore actuation behaviour at different excitation amplitudes, A, so as to identify the linear actuation regime, following Maia *et al.* (2021) and Maia *et al.* (2022). All the

f [Hz]	$M = 0.2$	$M = 0.25$	$M = 0.3$
[450, 700]	$St \approx [0.33, 0.51]$	$St \approx [0.26, 0.41]$	$St \approx [0.22, 0.34]$
[450, 1100]	$St \approx [0.33, 0.8]$	$St \approx [0.26, 0.64]$	$St \approx [0.22, 0.53]$
[450, 1500]	$St \approx [0.33, 1.09]$	$St \approx [0.26, 0.87]$	$St \approx [0.22, 0.73]$
[450, 2000]	$St \approx [0.33, 1.46]$	$St \approx [0.26, 1.16]$	$St \approx [0.22, 0.97]$

Table 1. Corresponding Strouhal number ranges to stochastic forcing excitation frequency bandwidths tested to characterise the actuator behaviour for the jet Mach numbers considered.

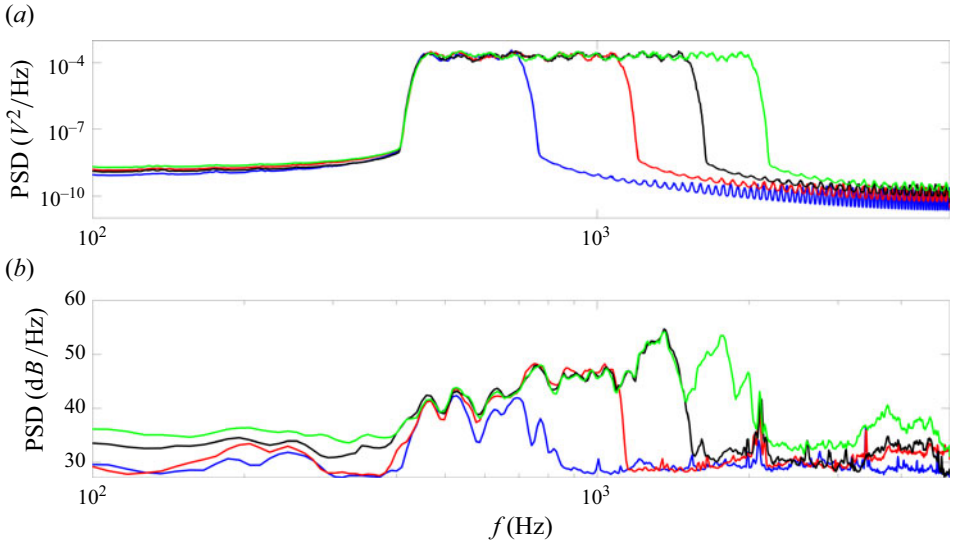

Figure 4. Actuator response to band-limited white noise excitation signal measured by the microphone in the acoustic field on the shielded side for different excitation frequency bands. (*a*) Excitation signal, (*b*) actuator response. Blue line refers to bandwidth $f = [450, 700]$ Hz, red line to $f = [450, 1100]$ Hz, black line to $f = [450, 1500]$ Hz, green line to $f = [450, 2000]$ Hz.

results shown below are obtained with the jet off. We excite the actuators with a band-limited stochastic forcing, that is, a band-pass filtered white noise, to explore different bandwidths and measure their response via the microphones in the acoustic field. We set the lowest excitation frequency to $f = 450$ Hz and consider different maximum excitation frequencies: $f = 700$ Hz, 1.1 kHz, 1.5 kHz and 2 kHz. The choice of the minimum excitation frequency was dictated by preliminary tests carried out using harmonic forcing signals that revealed that the actuators had a very weak response for $f < 400$ Hz. For the sake of brevity, these results are not reported herein. The corresponding Strouhal number ranges to the bandwidths tested for the M considered are reported in table 1, where the Strouhal number, St, is calculated based on nozzle diameter and jet velocity. Figure 4 shows the Power Spectral Density (PSD) on the shielded side for a given excitation amplitude. Consistent with the enlargement of the excited frequency band, the actuator response exhibits a spectrum with a non-zero amplitude on a larger frequency band. The actuators do not respond homogeneously throughout the excited frequency band.

We now explore the actuator behaviour for different excitation amplitudes, that is, $A = [0.5, 4]$ V. Figure 5 shows the standard deviation of the actuator response on the microphone on the shielded side as a function of the excitation amplitude. The standard

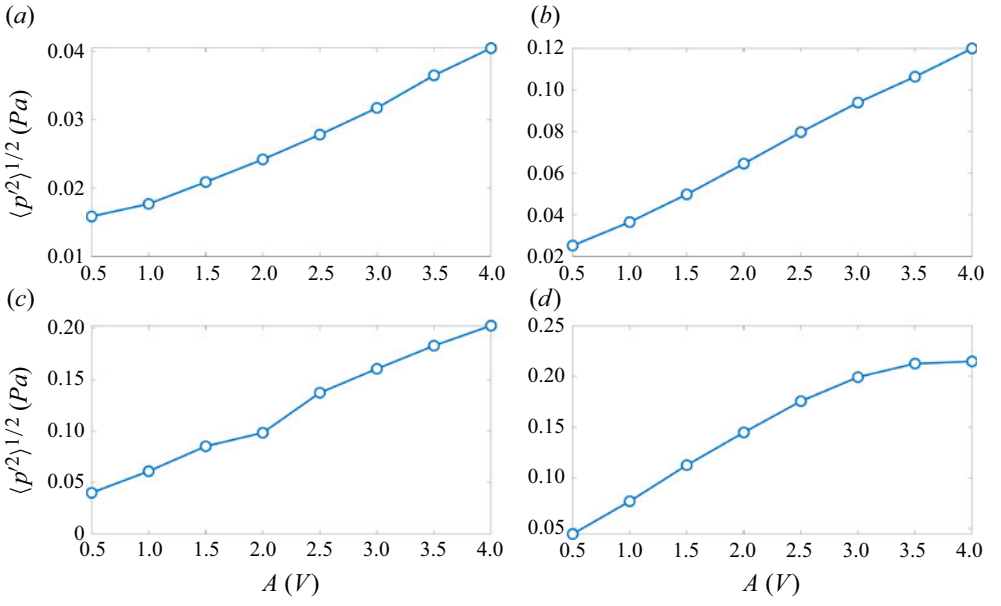

Figure 5. Standard deviation of the actuator response to band-limited white noise excitation signal measured by the pressure microphone in the acoustic field on the shielded side as a function of the excitation amplitude. (*a*) Excitation frequency band $f = [450, 700]$ Hz, (*b*) $f = [450, 1100]$ Hz, (*c*) $f = [450, 1500]$ Hz, (*d*) $f = [450, 2000]$ Hz.

deviation is calculated as the square root of the integral of the PSD response over the excited frequency band. As expected, the standard deviation amplitude increases as a consequence of the increase of the actuation bandwidth. We note that for the frequency range $f = [450, 2000]$ Hz the actuators tend to saturate at high amplitudes and start to behave nonlinearly. In light of this result, on the basis of the St-number range where JSI noise is dominant, that is, $St \approx [0.1, 0.8]$ (Mancinelli *et al.* 2022, 2024), and following the results of Maia *et al.* (2021) and Maia *et al.* (2022) where control effectiveness was shown to degrade for increasing actuation bandwidths, we select the bandwidth $f = [450, 1100]$ Hz as the operational frequency range of the actuators. All the results presented hereinafter are obtained using this operational frequency range.

We finally assess that the actuation forcing has a dipole behaviour in the operational frequency range, which is what is required, following the study of Karban *et al.* (2024), to control JSI noise. Figure 6 shows the absolute value of the phase of the cross-spectrum between the two microphones in the acoustic field on the shielded and unshielded sides, $\angle S_{\zeta_1\zeta_2}$, as a function of frequency at different excitation amplitudes. Except for the smallest excitation amplitudes, $A = 0.5$ and 1 V, where the actuator response was weak, the phase remains roughly constant around π over all the frequency band, thus implying a dipole source, as required. A slight departure from phase opposition is observed close to the maximum excitation frequency for all the amplitudes tested. However, this drawback does not affect control effectiveness, as it is shown in what follows.

4.2. *System identification*

The two control strategies involve two ingredients: estimation and actuation. In the estimation step, the noise radiated at the objective position, $\zeta(t)$, is provided via the TF $H_{\upsilon\zeta}$ from the near-field sensors $\upsilon(t)$. In the actuation step, the noise radiated in the acoustic field is zeroed, or at least reduced, based on the estimated ζ, assuming that

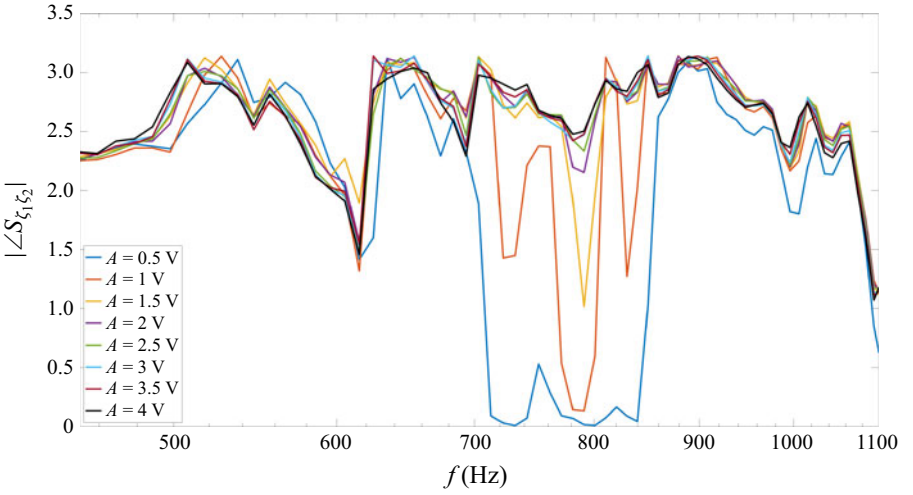

Figure 6. Phase between the two microphones in the acoustic field on the shielded and unshielded sides for actuation excitation signal equal to a band-limited stochastic forcing in the frequency band $f = [450, 1100]$ Hz at different excitation amplitudes.

the effect of the actuators on the observer and the potential contamination of the sensors by the actuators might be described by the TFs $H_{u\zeta}$ and $H_{u\upsilon}$, respectively.

We here identify the TFs between sensors, observer and actuators used to calculate the kernels for both the IFFC and the W–H control, according to (2.7) and (2.15), respectively. The TFs are estimated in two successive steps. First, the sensor-observer TF is identified via simultaneous readings of sensors and observer with the actuators off and calculated using (2.9*a*). Then, the actuator–sensor and actuator-observer TFs are identified forcing the actuators with a band-limited stochastic forcing in the range $f = [450, 1100]$Hz, performing simultaneous sensor–observer measurements. The TFs are calculated using (2.9*c*) and (2.9*b*). We note that the actuator–observer and actuator–sensor TF identification is not dependent on the type of forcing adopted. We chose a band-limited stochastic forcing for the present work for the sake of simplicity.

As mentioned above, the underlying assumption of the control strategy is linearity. We will use two-point coherence as a measure of the linearity of the system and as a means to characterise the TFs between sensors, observer and actuators. The accuracy of the estimation and actuation processes, and, thus, the control performance, is underpinned by the magnitude of the sensor–observer and actuator–observer coherence. The coherence between two generic time signals $a(t)$ and $b(t)$ is defined as

$$\gamma_{ab}(f) = \sqrt{\frac{|\langle S_{ab}(f)\rangle|^2}{|\langle S_{aa}(f)\rangle|\,|\langle S_{bb}(f)\rangle|}}. \tag{4.1}$$

4.2.1. *Estimation*

Figure 7 shows the PSDs of the axisymmetric pressure disturbance sensed by the near-field sensors, that successively constitutes the input for the controller, for both streamwise positions of the near-field array explored herein, $x/D = 0$ and $x/D = 1.7$. As an example, we show the results for jet Mach number $M = 0.2$. The $m = 0$ pressure mode is obtained as the average of the six near-field microphone readings along the azimuthal direction. The PSDs are presented hereinafter in $\mathrm{d}B/St$, according to the expression reported in what

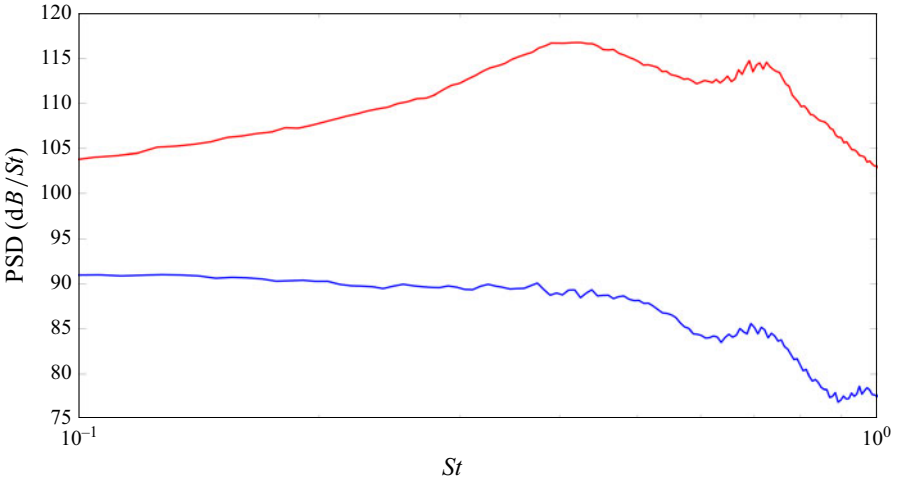

Figure 7. Spectra of near-field $m = 0$ mode for $M = 0.2$ in the case of unforced jet: blue line refers to $x/D = 0$ and red line to $x/D = 1.7$.

follows (Mancinelli *et al.* 2019; Pierce 2019)

$$\mathrm{PSD}\,[\mathrm{d}B/St] = 10\log_{10}\left(\frac{\mathrm{PSD}\,[Pa^2/Hz]}{p_{ref}^2}\frac{U_j}{D}\right), \tag{4.2}$$

where U_j is the jet velocity and $p_{ref} = 20\,\mu Pa$ is the reference pressure. The spectra change substantially with the streamwise position. As outlined by Mancinelli *et al.* (2024), the near-field sensors sense both the signature of the hydrodynamic wavepacket and the scattered acoustic pressure from the TE of the surface. Specifically, for array positions close to the nozzle exhaust the near-field sensors are dominated by the scattered acoustic pressure, whereas for positions downstream in the jet plume the hydrodynamic wavepacket signature becomes dominant. The physics just described explains the change of spectral shape observed in figure 7 and also affects control effectiveness, as will be shown in what follows. Figure 8 shows the coherence between the axisymmetric pressure mode educed by the near-field sensors and the noise at the observer position on the shielded side. We explore the effect on the coherence of both the streamwise position of the near-field sensors and the jet-flow conditions. For this aim, we consider both the streamwise positions investigated herein, $x/D = 0$ and $x/D = 1.7$, and the Mach numbers $M = 0.2$ and $M = 0.3$. The coherence exhibits high values for both flow conditions for $x/D = 1.7$ in the range $St \approx [0.1, 0.8]$ where jet installation noise is dominant. Concerning the effect of the streamwise position of the near-field array, we selected as flow condition $M = 0.2$ and note that the coherence is slightly larger for $x/D = 0$ than that measured for $x/D = 1.7$ due to the stronger significance of the scattered acoustic field close to the nozzle exhaust (Mancinelli *et al.* 2024). The coherence values are sufficiently high to accurately estimate the noise at the observer position and attempt noise control for both positions of the near-field array.

4.2.2. *Actuation*

Figure 9 shows the actuation effect on the near-field $m = 0$ pressure mode for jet Mach number $M = 0.2$ for both $x/D = 0$ and 1.7. We remind the reader that for these tests the jet was on and, following the characterisation of the actuators presented in § 4.1, we

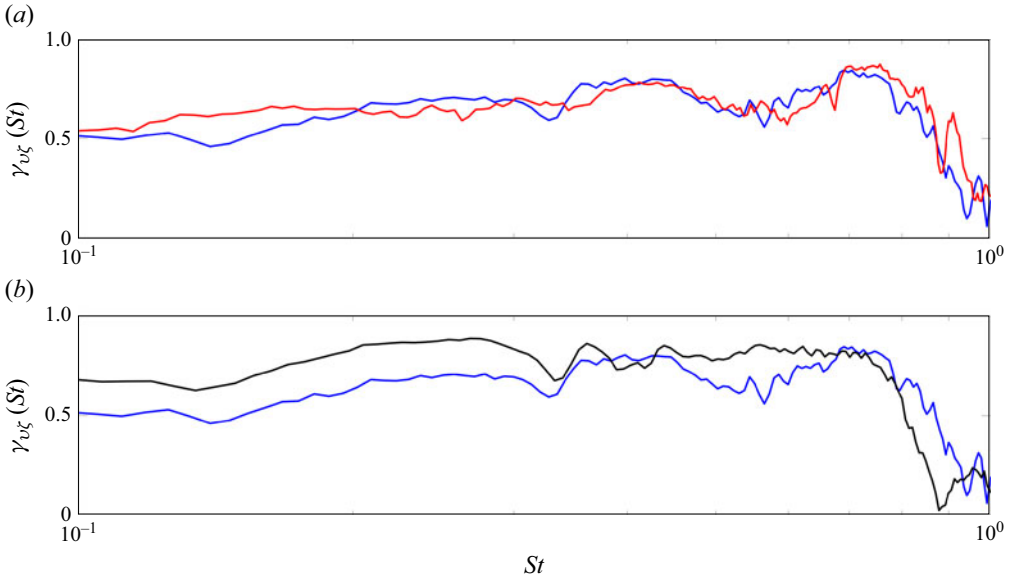

Figure 8. Sensor–observer coherence. (*a*) Effect of jet-flow conditions for the streamwise position of the near-field sensors $x/D = 1.7$: blue line refers to $M = 0.2$, red line to $M = 0.3$. (*b*) Effect of the streamwise position of the near-field sensors for $M = 0.2$: black line refers to $x/D = 0$, blue line to $x/D = 1.7$.

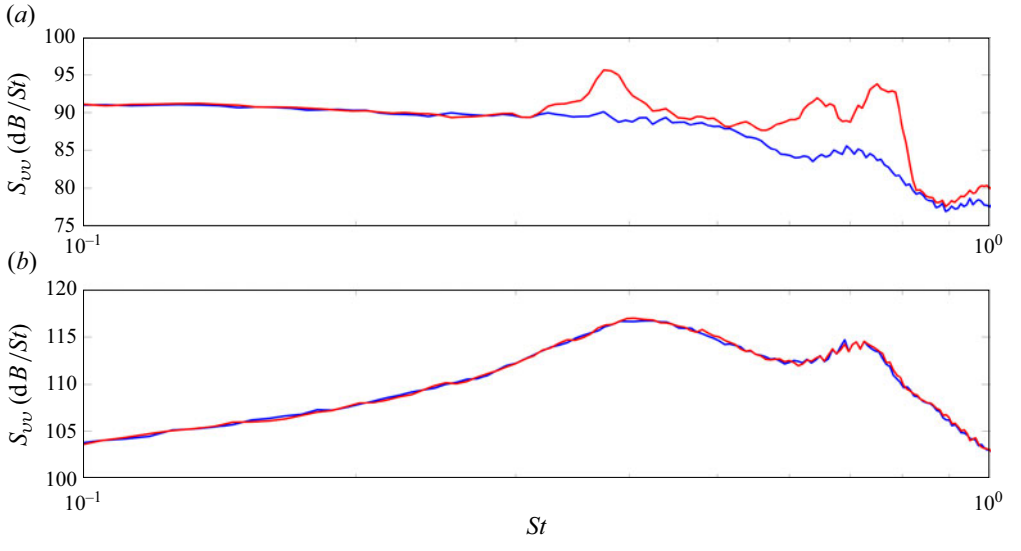

Figure 9. Actuation effect on near-field sensors for $M = 0.2$. Blue line refers to the spectrum with jet on and actuators off, red line to the spectrum with jet on and actuators forced with a band-limited stochastic forcing in the range $f = [450, 1100]$ Hz. (*a*) Streamwise position $x/D = 0$, (*b*) $x/D = 1.7$.

excited the actuators with a white noise band-pass filtered in the frequency range $f = [450, 1100]$ Hz, thus implying a St band of interest [0.33, 0.8] (see table 1). The actuation signature in the near-field sensor spectrum is clearly above the jet signature for $x/D = 0$, where the sensors mostly sense the acoustic pressure scattered by the TE of the plate. On the contrary, the sensors are less affected by the actuators when the array is moved

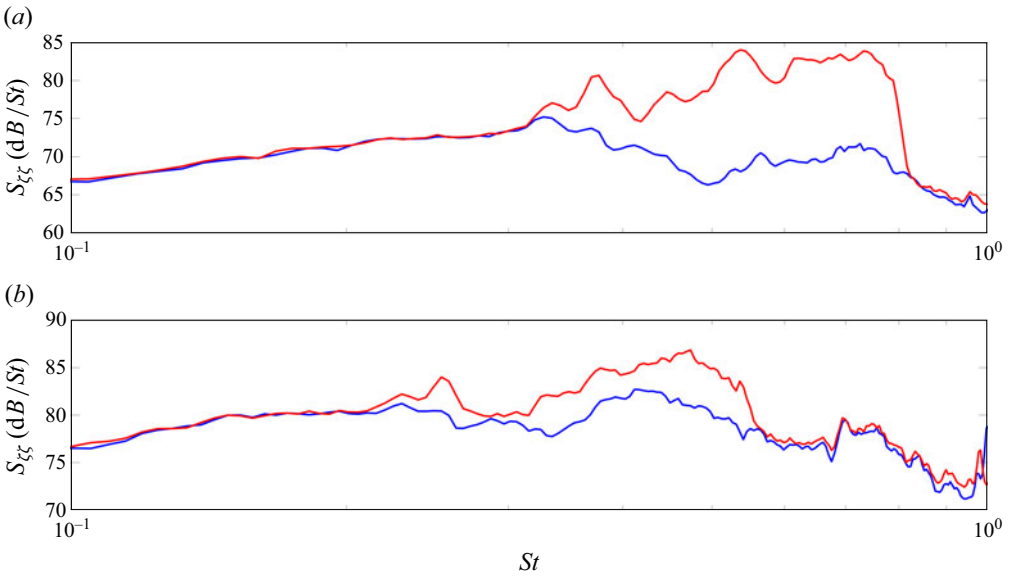

Figure 10. Actuation effect on observer on the shielded side of the acoustic field. Blue line refers to the spectrum with jet on and actuators off, red line to the spectrum with jet on and actuators forced with a band-limited stochastic forcing in the range $f = [450, 1100]$ Hz. (*a*) Jet Mach number $M = 0.2$, (*b*) $M = 0.3$.

further downstream in the jet plume and the hydrodynamic pressure field generated by the jet becomes dominant. The actuation effect on the observer on the shielded side for $M = 0.2$ and 0.3 is shown in figure 10. We note that the actuation signature in the spectrum becomes less evident for increasing M and the noise emitted by the jet dominates over that generated by the actuators. For the control to be efficient, the actuation signature needs to emerge above the jet signature, since this ensures that the actuators have sufficient energy to generate pressure fluctuations comparable to those created by the jet, thus being strong enough to cancel them. We thus expect a reduction in control effectiveness at high M.

The actuator–sensor and actuator–observer coherence is shown in figure 11. The coherence between the actuator and the observer is decreased with increasing Mach number. Where the actuator-to-sensor coherence is concerned, for the downstream sensor position, $x/D = 1.7$, the coherence drops to zero for both Mach numbers. This is because the hydrodynamic signature of coherent structures here largely dominates the signature of the scattered sound field, leading to a low signal-to-noise ratio between actuator and sensor, where 'noise' can be here interpreted as the hydrodynamic component of the measurement. On the contrary, the large value of $\gamma_{u\upsilon}$ for $x/D = 0$ implies a significant contamination of the sensor readings by the actuators that might lead to Larsen effect (Sanfilippo & Valle 2013) for high actuation amplitudes; this aspect will be taken into account by the actuator–sensor TF $H_{u\upsilon}$ in the control-kernel calculation according to (2.7) and (2.15).

4.3. *Control*

4.3.1. *Kernel calculation*

In order to prevent undesired noise captured by the sensors/observer from affecting the kernel, a zero-phase band-pass filter for the frequency band for which the actuators were forced was applied to the raw data before the calculation of the TFs. Following Audiffred *et al.* (2024*b*), a constant term ϵ was added to the PSDs of u and υ to regularise the

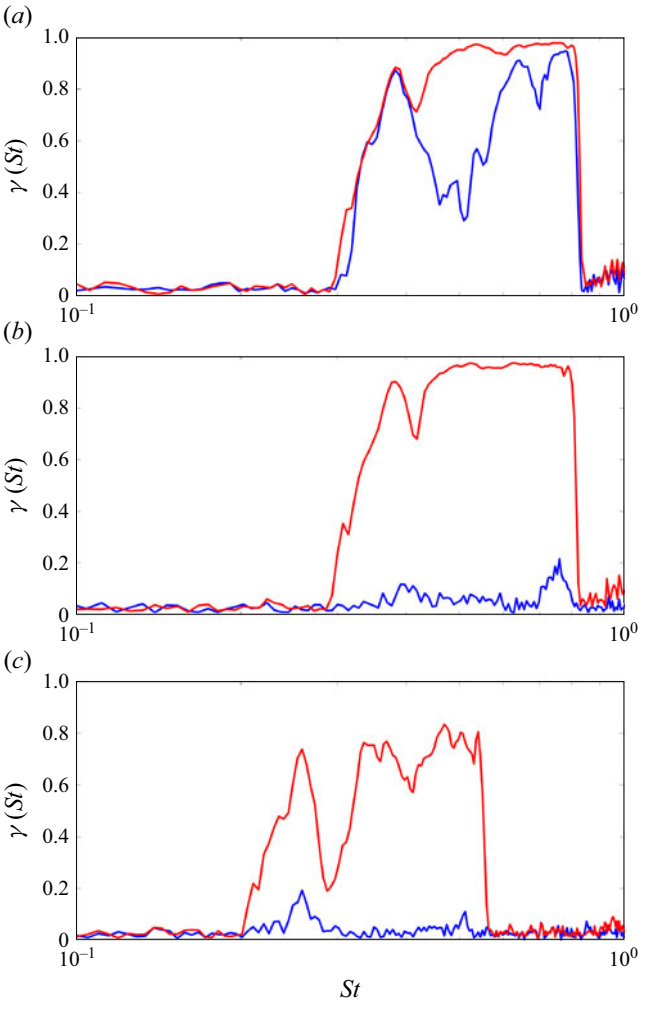

Figure 11. Actuator–sensor (blue lines) and actuator–observer (red lines) coherence functions for jet-flow conditions $M = 0.2$ and 0.3 and streamwise positions of near-field sensor array $x/D = 0$ and $x/D = 1.7$. Panels show (*a*) $x/D = 0$ and $M = 0.2$, (*b*) $x/D = 1.7$ and $M = 0.2$, (*c*) $x/D = 1.7$ and $M = 0.3$.

problem and avoid divisions by zero (or values close to zero) in the TF calculation in (2.9) and, thus, in the kernel calculation in (2.7) and (2.15). Choosing ϵ a couple of orders of magnitude lower than the typical value of the PSD in the frequency band of interest ensures a proper regularisation of the calculation and that the TFs are well approximated in the frequency band. Values of ϵ of 10^{-6} and 10^{-5} were used for S_{uu} and $S_{\upsilon\upsilon}$, respectively.

We first explore the effect of the penalisation factor R used for the kernel calculation in (2.7) and (2.13*a*) on the control effectiveness to identify the value R that maximises noise reduction. To do so, we iteratively calculate the control kernel for both the IFFC and W–H control for different values of R and implement an off-line control. Following the expression in (2.11), the controlled observer signal in the time domain can be estimated as the linear superposition of the open-loop behaviour and the actuation effect

$$\zeta_c(t) = \zeta_{unc}(t) + h_{u\zeta}(t) * u(t) = (h_{\upsilon\zeta}(t) + h_{u\zeta}(t) * k(t)) * \upsilon(t), \tag{4.3}$$

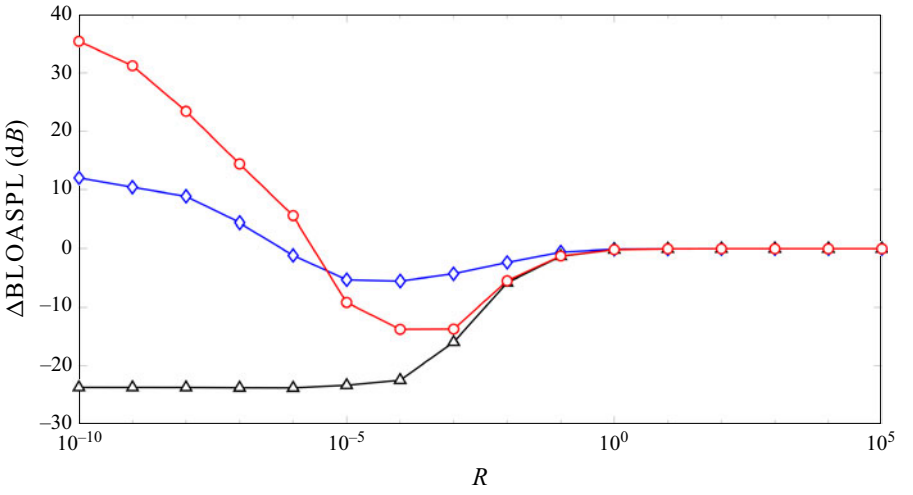

Figure 12. Noise reduction achieved in the off-line control for $M = 0.2$ and near-field sensors at $x/D = 1.7$. Blue $\diamond$ symbols refer to results obtained using the truncated, causal IFFC kernel, red $\circ$ to W–H control kernel, black $\triangle$ to non-causal kernel.

where $h_{v\zeta}$ is the sensor–observer TF in the time domain. Figure 12 shows the band-limited over-all sound pressure level difference, ΔBLOASPL, between the controlled and uncontrolled observer signals as a function of the penalisation factor R used to compute the control kernel. As an example, we show the results for $M = 0.2$ and the near-field sensors at $x/D = 1.7$. The BLOASPL is calculated using the formula

$$\text{BLOASPL} = 20 \log_{10} \frac{\sigma}{p_{ref}}, \tag{4.4}$$

where σ is the standard deviation of the controlled/uncontrolled signal. The standard deviation is calculated from the variance σ^2, which is estimated as

$$\sigma^2 = \int_{f_1}^{f_2} \text{PSD}(f)\, \mathrm{d}f, \tag{4.5}$$

where f_1 and f_2 correspond to the minimum and maximum forcing frequencies of the actuators, that is, 450 Hz and 1.1 kHz, respectively. We compare the noise reduction achieved in the off-line tests using the control kernel obtained for both the W–H and the IFFC approaches as well as using the non-causal kernel, as formalised in (2.2). The non-causal kernel provides the largest noise reductions, but, as discussed above, this implies the actuation dependence on sensor readings in the future, which is not feasible in real applications. As expected, the achievable noise reductions tend to zero for $R \to \infty$ for all the kernels considered and this is related to the fact that the actuation effect on the observer becomes negligible for high control penalisation values. We note that there exists a range of penalisation factor values for which the W–H and the IFFC approaches exhibit high effectiveness, the W–H control being more effective. The range of optimal penalisation values is slightly different between the IFFC and W–H control. Specifically, the largest noise reductions are achieved for $R = [10^{-5}, 10^{-4}]$ and $R = [10^{-4}, 10^{-3}]$ for the IFFC and the W–H control, respectively. Hence, the R values are chosen within these ranges for the two controllers. We note that in the W–H framework the noise reduction trend for increasing values of the penalisation factor should be monotonically decreasing

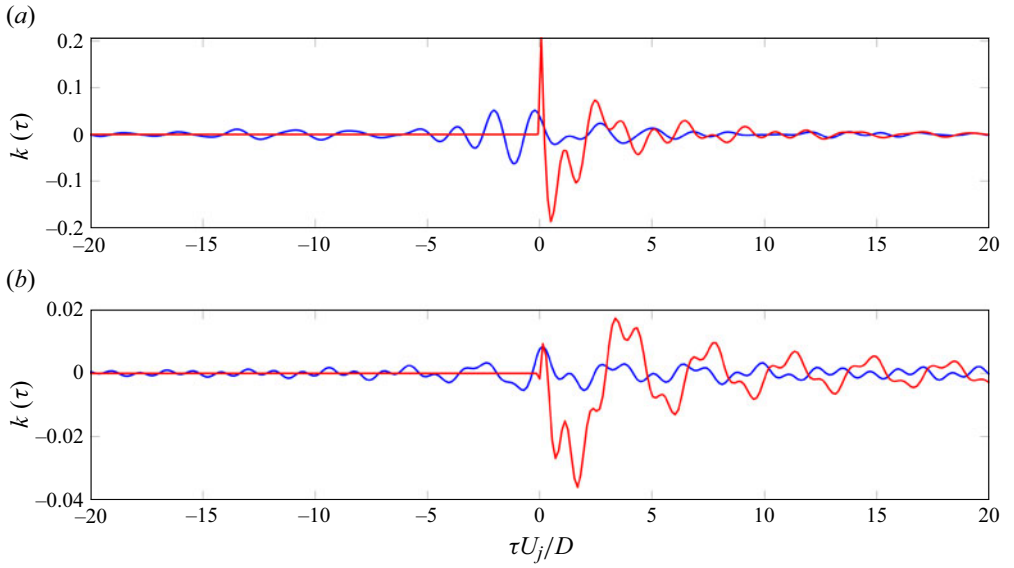

Figure 13. Control kernels for IFFC (blue lines) and W–H (red lines) approaches for $M = 0.2$: (*a*) near-field sensors at $x/D = 0$, (*b*) $x/D = 1.7$.

(Martini *et al.* 2022). The performance loss for low R values is likely related to a low signal-to-noise ratio, the undesired measurement noise captured by the sensors and the observer being larger than R.

Figure 13 shows the IFFC and W–H control kernels for $M = 0.2$ and R values of 10^{-4} and 10^{-3}, respectively, for both the streamwise positions of near-field sensors, $x/D = 0$ and $x/D = 1.7$. The non-causal part of the IFFC kernel is much more significant at $x/D = 0$ than at $x/D = 1.7$. This is consistent with the physics described above and with the results presented by Mancinelli *et al.* (2024), where the sensor–observer coherence was shown to be dominated by the acoustic pressure scattered by the TE of the surface. The higher significance of the non-causal part at $x/D = 0$ is further supported by the larger peak of the W–H kernel for $\tau \approx 0$ for such streamwise position, which is how the W–H kernel compensates for the anti-causal part.

4.3.2. *Control results*

Figure 14 shows the control results at the objective position on the shielded side for $M = 0.2$ and near-field sensors placed at $x/D = 0$ and $x/D = 1.7$ for both the IFFC and W–H kernels. In order to prove control authority, we compare the uncontrolled case with controlled cases using both the reduction and amplification kernels The reduction kernels are obtained using (2.7) and (2.15) for the IFFC and W–H, respectively, whereas the amplification kernel is obtained by multiplying the reduction kernel by -1 to create a dipole that interferes constructively, instead of destructively, with the waves scattered at the TE. We note that noise control is achieved for both streamwise positions of the near-field sensors and for both the IFFC and W–H kernels over the whole frequency range we sought to control. Noise control is more effective for $x/D = 1.7$ and using the W–H kernel. The dependence of the control performance on the sensor position is essentially related to the nature of the pressure disturbances measured by the near-field sensors. Control is more effective for positions where the hydrodynamic component related to the convected

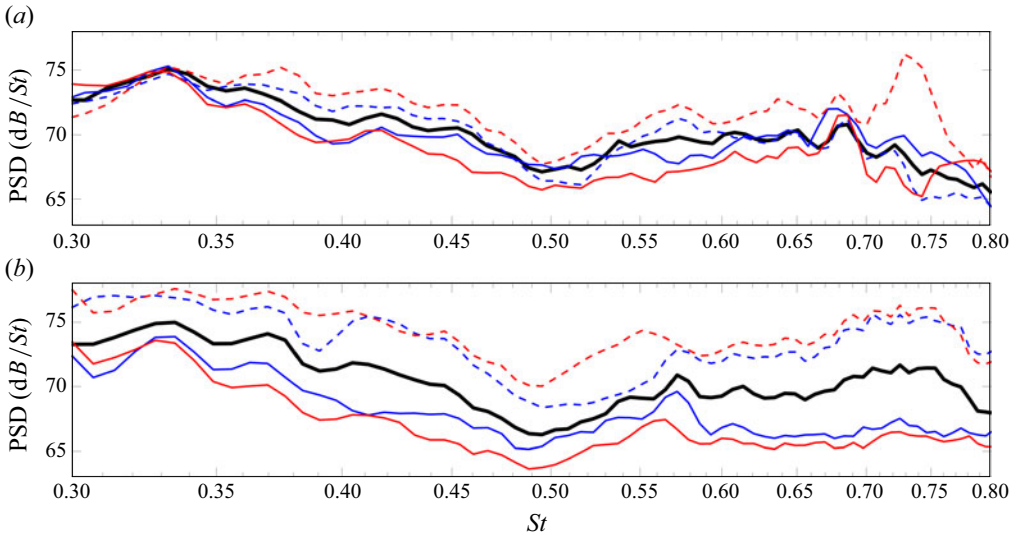

Figure 14. Noise control at the objective position on the shielded side of the acoustic field for $M = 0.2$ and near-field sensors at $x/D = 0$ and $x/D = 1.7$: (*a*) $x/D = 0$, (*b*) $x/D = 1.7$. Reduction and amplification kernels are used for both the IFFC and W–H controls: bold black lines refer to the uncontrolled case, blue lines to IFFC, red lines to W–H. Solid lines refer to results obtained using the reduction kernel, dashed lines to the amplification kernel.

wavepacket dominates the sensor reading, that is, for downstream positions in the jet plume of the near-field array. Nevertheless, consistent with the results obtained by Bychkov *et al.* (2019) and Kopiev *et al.* (2020), where jet installation noise was successfully controlled using wave cancellation in a feedback scheme, and as suggested by Sipp & Schmid (2016), actuators have a certain effectiveness and control is achieved at $x/D = 0$ even if most of the IFFC kernel information is non-causal due to a certain spatio-temporal coherence of the scattering wavepacket.

The higher effectiveness of the W–H control with respect to the IFFC is apparent for both the streamwise positions of near-field sensors considered. This result is consistent with what was found by Audiffred *et al.* (2023) for the control of Tollmien–Schlichting waves over a wing profile. The maximum noise reductions and amplifications and the ΔBLOASPL achieved with both the IFFC and W–H kernels for both the streamwise positions of sensors are visualised in figure 15.

We now explore the effect of jet-flow conditions on the control effectiveness. We carried out this analysis only for the streamwise position of the near-field sensors where we obtained the largest noise reductions/amplifications, that is, $x/D = 1.7$. Figure 16 shows the PSD at the objective position on the shielded side of the acoustic field for $M = 0.2$, 0.25 and 0.3. Consistent with what has been shown above, we compare the spectra of the uncontrolled case with the results obtained using both the IFFC and W–H and both the amplification and reduction kernels. As outlined above, we kept the actuation frequency range fixed in the band where the actuators were found to be more effective. As a consequence, the Strouhal number range in which control is achieved is different for the M explored. Noise control is achieved over all of the actuation frequency range and for all jet-flow conditions. We note that the control effectiveness is slightly higher at high frequencies, where the actuators showed the largest response (cf. figure 4), and reduces with increasing M. The degradation of the control efficiency with increasing M

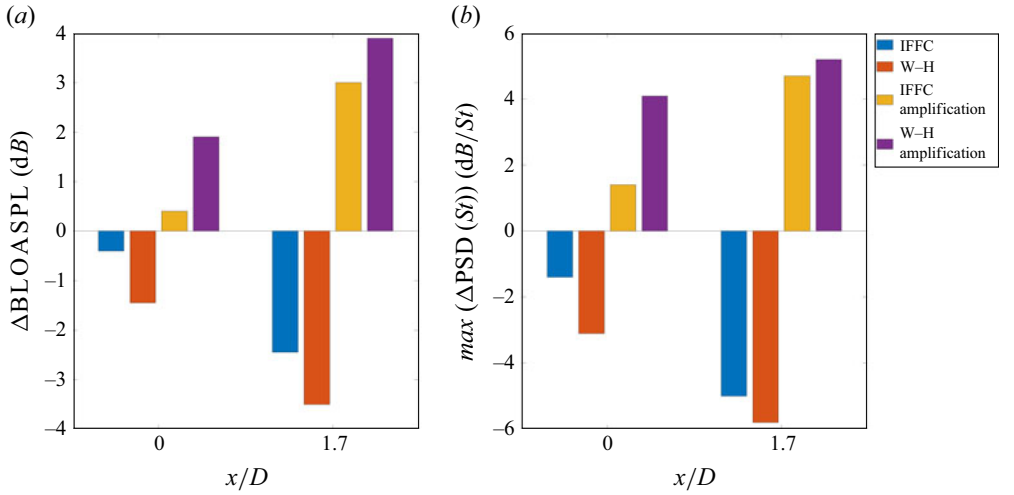

Figure 15. Noise reductions and amplifications with respect to the uncontrolled case at the observer position obtained using both IFFC and W–H approaches for $M = 0.2$ and streamwise positions of near-field sensors $x/D = 0$ and $x/D = 1.7$. (*a*) Band-limited OASPL difference, (*b*) maximum spectral amplitude difference at a given St.

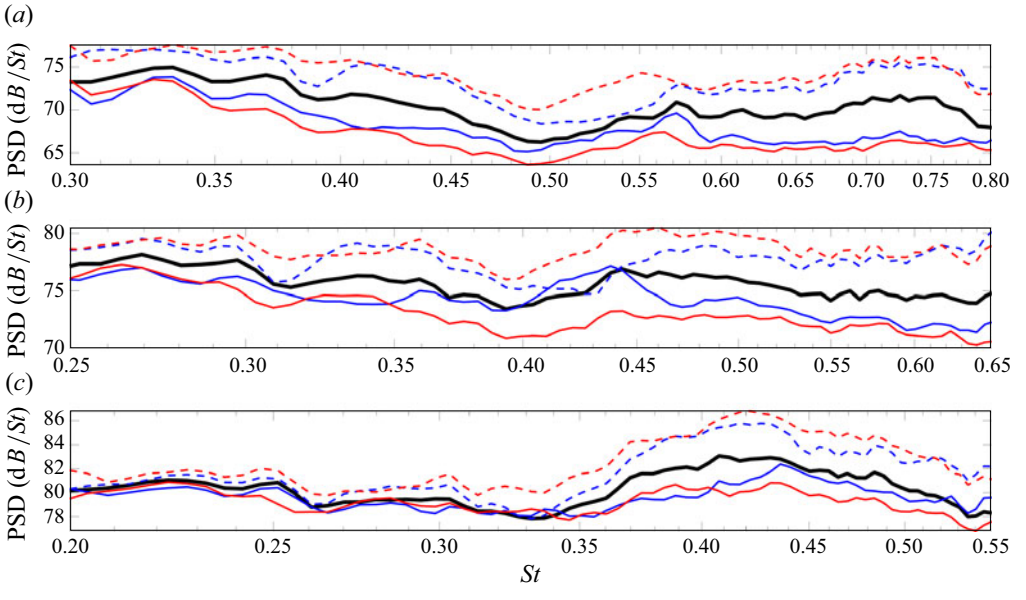

Figure 16. Mach effect on noise control effectiveness for near-field sensors at streamwise position $x/D = 1.7$: (*a*) $M = 0.2$, (*b*) $M = 0.25$, (*c*) $M = 0.3$. Reduction and amplification kernels are used for both the IFFC and W–H controls: bold black lines refer to the uncontrolled case, blue lines to IFFC, red lines to W–H. Solid lines refer to results obtained using the reduction kernel, dashed lines to the amplification kernel.

is quantified in figure 17, where the maximum noise reductions/amplifications and the ΔBLOASPL with respect to the uncontrolled case are reported. The higher performance of the W–H approach than that of the IFFC is evident for all the jet-flow conditions considered herein.

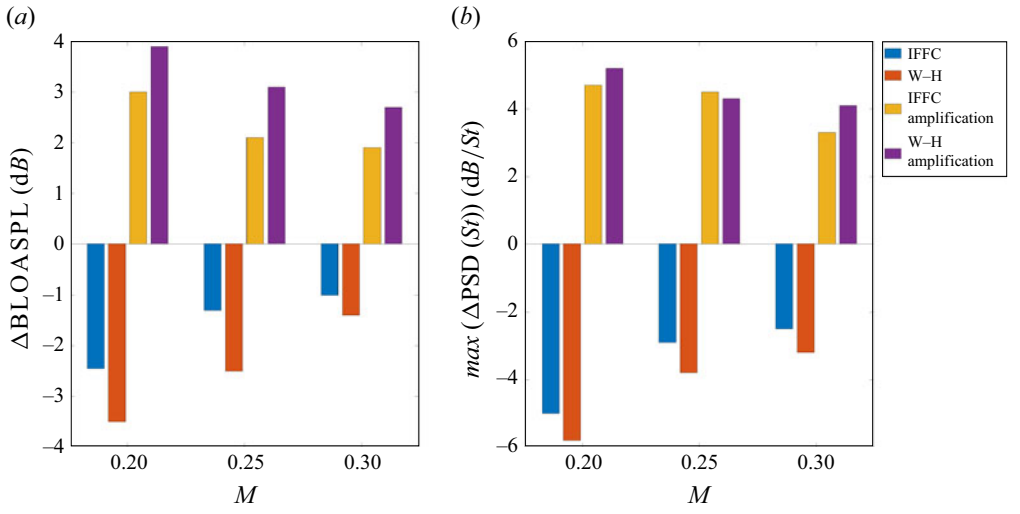

Figure 17. Noise reductions and amplifications with respect to the uncontrolled case at the observer position obtained using both the IFFC and W–H approaches for $x/D = 1.7$ and $M = 0.2$, 0.25 and 0.3. (*a*) Band-limited OASPL difference, (*b*) maximum spectral amplitude difference at a given St.

5. Conclusions

We presented an experimental study of real-time, linear reactive control of jet installation noise. We considered a set-up where a flat plate is installed parallel to the nozzle axis of a subsonic turbulent jet at a Reynolds number of $[2.2, 3.4] \times 10^5$. The configuration is intended to be a simplified representation of a jet–wing interaction. In this configuration, JSI noise is underpinned by the scattering of turbulent wavepackets by the TE of the surface. The control strategy is based on wave cancellation and involves the use of near-field sensors to drive edge-mounted actuators to control the noise radiation. The near-field sensors and the observer in the acoustic field consist of a 6-microphone azimuthal array to educe the $m = 0$ pressure disturbances and a microphone located in the shielded region of the acoustic field, respectively, and the actuators are piezoelectric patches. Following the results obtained by Karban *et al.* (2024) in a simplified model, the control mechanism amounts to the imposition of an edge dipole driven in phase opposition to the jet-edge-interaction dipole. Two control strategies were tested: (i) IFFC (Maia *et al.* 2021, 2022) and (ii) W–H control (Martini *et al.* 2022; Audiffred *et al.* 2024*b*). Both approaches are based on measured TFs. Based on the results presented by Mancinelli *et al.* (2024), where optimal sensor positioning for implementation of closed-loop control of JSI noise was assessed via the investigation of the effectiveness of noise estimation based on near-field sensor readings, we implemented control for two streamwise positions of the near-field sensors, $x/D = 0$ and $x/D = 1.7$. We showed that control efficiency depends on sensor positioning due to the stronger relative presence of the scattered sound field in upstream sensor measurements where the hydrodynamic signature of the convecting coherent structures is weak. Noise control was successfully achieved using both IFFC and W–H approaches and we showed that the W–H approach generates the largest noise reductions/amplifications. The OASPL reductions and amplifications over all the actuation frequency range of up to 3.5 and 4 dB, respectively, and a maximum noise reduction/amplification of up to 6 dB/St were achieved at $x/D = 1.7$ using the W–H approach.

Future developments of the present activity will involve an improvement of the actuation technology to test reactive control at higher jet velocities and the exploration of control robustness to jet-flow condition variations. We finally note that for the present academic study we were not interested in assessing the control cost, but rather in addressing the question whether broadband control was possible. The assessment of the control applicability considering the control effort as a constraint will be the objective of future studies.

Acknowledgements. The authors acknowledge R. Kari for his support in the design of the experimental set-up.

Funding. M.M. and P.J. acknowledge the support of the EU project DJINN funded by the European Union's Horizon 2020 research and innovation programme under grant agreement No 861438. D.A. acknowledges the financial support from the São Paulo Research Foundation (FAPESP), grants 2022/03279-5 and 2019/26546-6.

Declaration of interests. The authors report no conflict of interest.

Appendix A. Wiener–Hopf approach

The W–H formalism is adopted for problems where a half-domain condition needs to be satisfied (Noble & Weiss 1959), such as the following half-convolution problem:

$$\boldsymbol{b}\,(t) = \int_0^{+\infty} \boldsymbol{w}_+\,(\tau)\,\boldsymbol{s}\,(t-\tau)\;\mathrm{d}\tau \qquad t > 0, \tag{A1}$$

where $\boldsymbol{w}$ is an unknown function and $\boldsymbol{s}$ and $\boldsymbol{b}$ are known functions which in the jet installation noise control framework presented herein are related to the sensor and actuation signals, respectively. Extending this equation to $t < 0$ leads to the W–H equation (Noble & Weiss 1959) in the frequency domain

$$\boldsymbol{S}(f)\boldsymbol{W}_+(f) = \boldsymbol{W}_-(f) + \boldsymbol{B}_+(f), \tag{A2}$$

where the subscripts $+$ and $-$ indicate that the associated functions are analytical in the upper and lower complex half-planes, respectively. This is ensured for $\boldsymbol{W}_-$ and $\boldsymbol{W}_+$ given that these functions are zero for positive and negative times, respectively. The solution of the problem described by (A1) is found by using the multiplicative and additive factorisations (Daniele & Lombardi 2007) defined in the following:

$$\boldsymbol{S}(f) = \boldsymbol{S}_-(f)\boldsymbol{S}_+(f), \tag{A3a}$$

$$\boldsymbol{S}_-{}^{-1}(f)\boldsymbol{b}_+ = \left(\boldsymbol{S}_-{}^{-1}(f)\boldsymbol{b}_+(f)\right)_+ + \left(\boldsymbol{S}_-{}^{-1}(f)\boldsymbol{b}_+(f)\right)_-, \tag{A3b}$$

which lead to the solution (Audiffred *et al.* 2023)

$$\boldsymbol{W}_+(f) = \boldsymbol{S}_+{}^{-1}(f)(\boldsymbol{S}_-{}^{-1}(f)\boldsymbol{B}(f))_+, \tag{A4a}$$

$$\boldsymbol{W}_-(f) = -\boldsymbol{S}_-(f)(\boldsymbol{S}_-{}^{-1}(f)\boldsymbol{B}(f))_-. \tag{A4b}$$

Appendix B. Control results on the unshielded side

We here explore jet installation noise control on the unshielded side. We carried out this analysis only for the streamwise position of the near-field sensors where we obtained the largest noise reductions/amplifications, that is, $x/D = 1.7$. Figure 18 shows uncontrolled and controlled noise spectra for $M = 0.2$ on the unshielded side using both IFFC and W–H approaches. Control results are consistent with those found on the shielded side, the W–H approach being more effective than IFFC. We note that control effectiveness

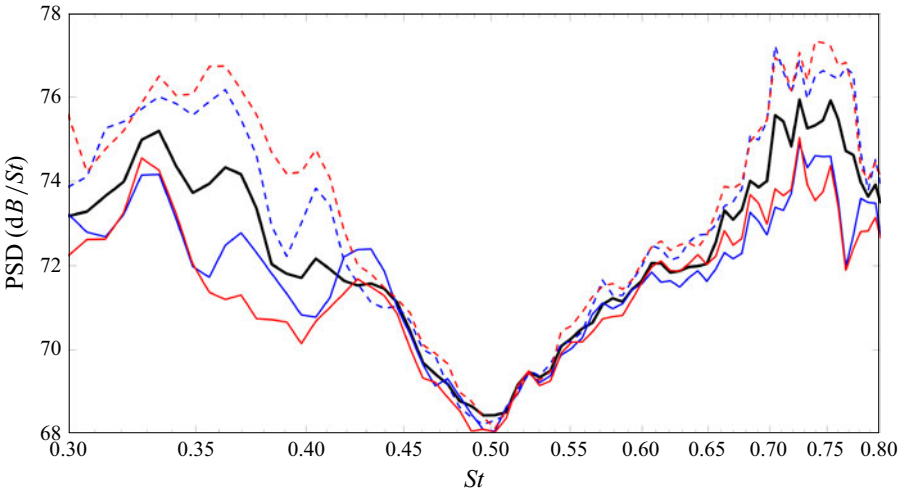

Figure 18. Noise spectra on the unshielded side for $M = 0.2$ and near-field microphone array at $x/D = 1.7$. Reduction and amplification kernels are used for both IFFC and W–H approaches. Bold black line refers to the uncontrolled case, blue lines to IFFC and red lines to W–H: solid lines refer to results using the reduction kernel, dashed lines to the amplification kernel.

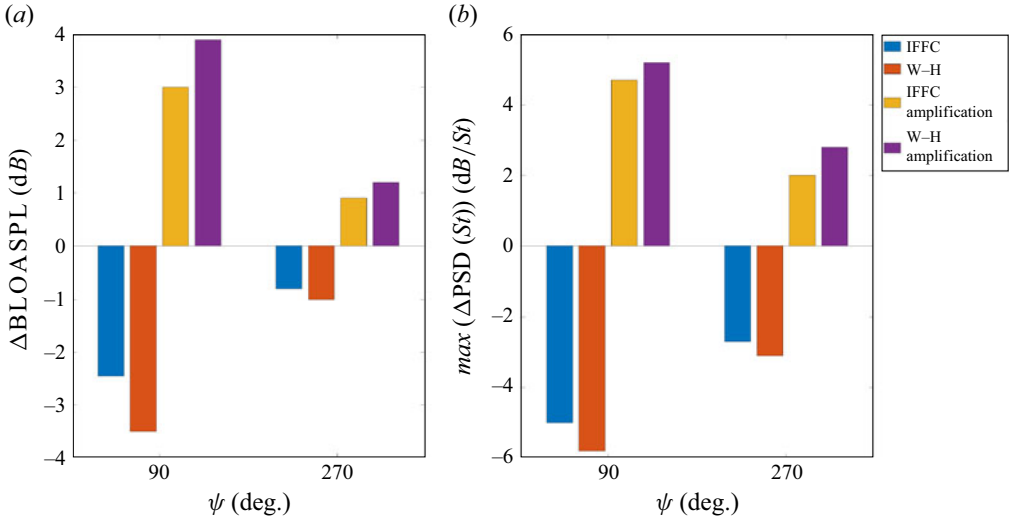

Figure 19. Comparison between noise reductions and amplifications with respect to the uncontrolled case achieved on the shielded and unshielded sides ($\psi = 90°$ and $270°$) using both IFFC and W–H for $M = 0.2$ and near-field sensors at $x/D = 1.7$. (*a*) Band-limited OASPL difference, (*b*) maximum spectral amplitude difference at a given St.

is lower than that achieved on the shielded side. As mentioned in § 3, this behaviour is likely due to the influence of direct jet noise, whose physical mechanism is different from JSI noise and cannot be controlled with the application developed herein, and flow–sound interactions, such as refraction and scattering by turbulence. The comparison of control authority between the shielded and unshielded sides is quantified in figure 19, where we show the maximum noise reductions and amplifications and the ΔBLOASPL with respect to the uncontrolled case achieved in both regions of the acoustic field. The shielded and

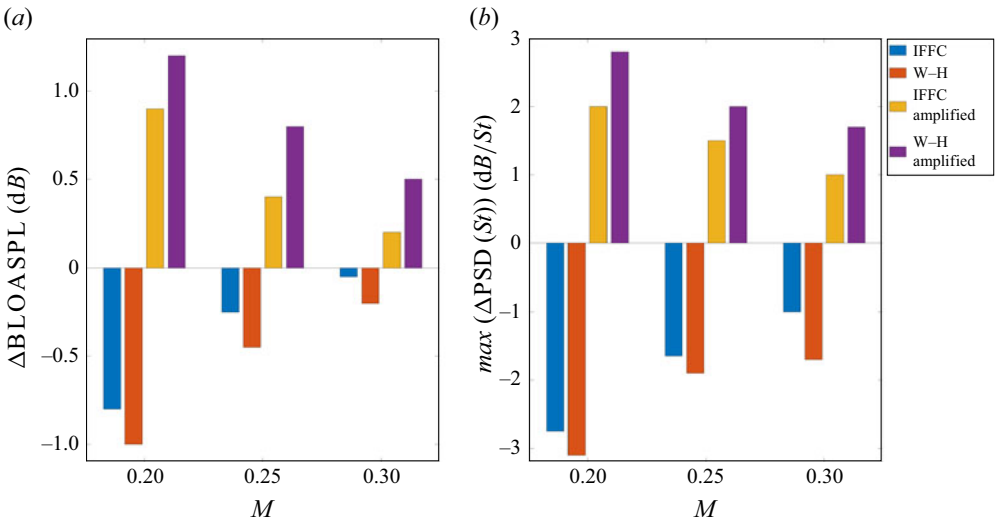

Figure 20. Noise reductions and amplifications with respect to the uncontrolled case on the unshielded side as a function of M using both IFFC and W–H approaches for near-field sensors at $x/D = 1.7$. (*a*) Band-limited OASPL difference, (*b*) maximum spectral amplitude difference at a given St.

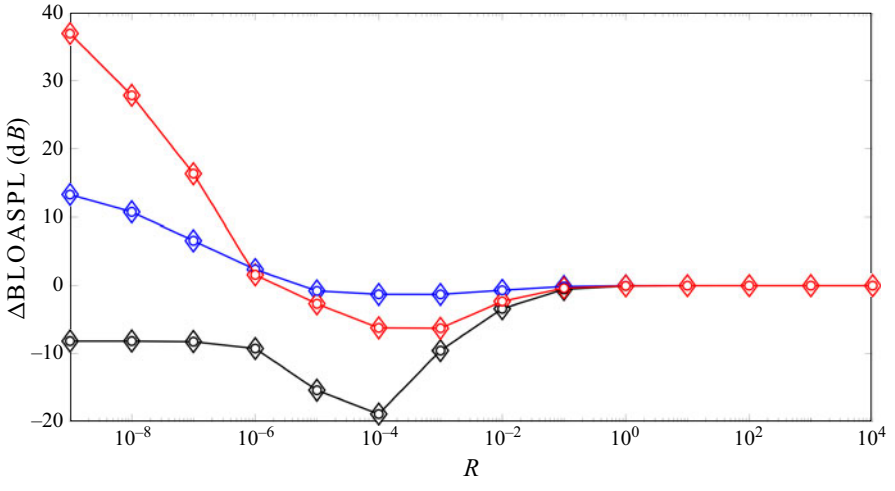

Figure 21. Noise reduction achieved on the unshielded side in the off-line control for $M = 0.2$ and near-field sensors at $x/D = 1.7$. Blue lines refer to causal IFFC, black lines to non-causal kernel, red lines to W–H. Big ◇ symbols refer to results obtained using the microphone on the unshielded side to calculate the kernel, ○ to the microphone on the shielded side to calculate the kernel.

unshielded sides are identified via the polar angle $\psi = 90°$ and $\psi = 270°$, respectively. Control effectiveness is reduced of 40 %–50 % on the unshielded side with respect to the shielded side.

The effect of jet-flow conditions on control effectiveness on the unshielded side is explored in figure 20, where we show the maximum noise reductions/amplifications and the ΔBLOASPL with respect to the uncontrolled case for all M considered herein. The degradation of control efficiency with increasing M is consistent with what observed on the shielded side (cf. figure 17).

We note that the control results on the unshielded side shown above are obtained using the microphone on the shielded side as observer to calculate the control kernel. To explore whether the choice of the microphone used to calculate the kernel might affect the control effectiveness, we consider the off-line control and compare the noise reductions achieved on the unshielded side using both the microphones on the shielded and unshielded sides to estimate the kernel. The results are shown in figure 21 as a function of the penalisation factor R and reveal that the choice of the observer for kernel estimation either on the shielded or unshielded side does not affect control authority.

References

Åkervik, E., Hœpffner, J., Ehrenstein, U.W.E. & Henningson, D.S. 2007 Optimal growth, model reduction and control in a separated boundary-layer flow using global eigenmodes. *J. Fluid Mech.* **579**, 305–314.

Audiffred, D., Mancinelli, M., Cavalieri, A.V.G., Martini, E. & Jordan, P. 2024*a* Experimental control of jet installation noise. In 30th AIAA/CEAS Aeroacoustics Conference, pp. 3314. AIAA Paper.

Audiffred, D.B.S., Cavalieri, A.V.G., Maia, I.A., Martini, E. & Jordan, P. 2024*b* Reactive experimental control of turbulent jets. *J. Fluid Mech.* **994**, A15.

Audiffred, D.B.S., Cavalieri, A.V.G., Brito, P.P.C. & Martini, E. 2023 Experimental control of Tollmien–Schlichting waves using the Wiener–Hopf formalism. *Phys. Rev. Fluids* **8** (7), 073902.

Bagheri, S., Henningson, D.S., Hoepffner, J. & Schmid, P.J. 2009 Input–output analysis and control design applied to a linear model of spatially developing flows. *Appl. Mech. Rev.* **62**, 020803.

Barbagallo, A., Dergham, G., Sipp, D., Schmid, P.J. & Robinet, J.C. 2012 Closed-loop control of unsteadiness over a rounded backward-facing step. *J. Fluid Mech.* **703**, 326–362.

Barbagallo, A., Sipp, D. & Schmid, P.J. 2009 Closed-loop control of an open cavity flow using reduced-order models. *J. Fluid Mech.* **641**, 1–50.

Bendat, J.S. & Piersol, A.G. 2011 *Random Data: Analysis and Measurement Procedures*. John Wiley & Sons.

Brito, P.P.C., Morra, P., Cavalieri, A.V.G., Araújo, T.B., Henningson, D.S. & Hanifi, A. 2021 Experimental control of Tollmien–Schlichting waves using pressure sensors and plasma actuators. *Exp. Fluids* **62**, 1–13.

Brown, C.A. 2013 Jet-surface interaction test: far-field noise results. *J. Engng Gas Turbines Power* **135** (7), 071201.

Bychkov, O.P., Faranosov, G., Kopiev, V., Kopiev, V.A., Moralev, I. & Kazansky, P. 2019 Plasma-based active closed-loop control of instability waves in unexcited turbulent jet. Part 2. Installed jet. In *25th AIAA/CEAS Aeroacoustics Conference*, pp. 2019–2558. AIAA paper.

Cavalieri, A.V.G. & Agarwal, A. 2014 Coherence decay and its impact on sound radiation by wavepackets. *J. Fluid Mech.* **748**, 399–415.

Cavalieri, A.V.G., Jordan, P., Agarwal, A. & Gervais, Y. 2011 Jittering wave-packet models for subsonic jet noise. *J. Sound Vib.* **330** (18-19), 4474–4492.

Cavalieri, A.V.G., Jordan, P., Colonius, T. & Gervais, Y. 2012 Axisymmetric superdirectivity in subsonic jets. *J. Fluid Mech.* **704**, 388–420.

Cavalieri, A.V.G., Jordan, P. & Lesshafft, L. 2019 Wave-packet models for jet dynamics and sound radiation. *Appl. Mech. Rev.* **71** (2), 020802.

Cavalieri, A.V.G., Jordan, P., Wolf, W.R. & Gervais, Y. 2014 Scattering of wavepackets by a flat plate in the vicinity of a turbulent jet. *J. Sound Vib.* **333** (24), 6516–6531.

Cavalieri, A.V.G., Rodríguez, D., Jordan, P., Colonius, T. & Gervais, Y. 2013 Wavepackets in the velocity field of turbulent jets. *J. Fluid Mech.* **730**, 559–592.

Daniele, V. & Lombardi, G. 2007 Fredholm factorization of Wiener–Hopf scalar and matrix kernels. *Radio Sci.* **42** (06), 1–19.

Faranosov, G., Bychkov, O.P., Kopiev, V., Soares, L.F. & Cavalieri, A.V.G. 2019 The modeling of jet-plate interaction noise in the presence of co-flow. In *25th AIAA/CEAS Aeroacoustics Conference. AIAA Paper 2492-2019*. American Institute of Aeronautics and Astronautics.

Jaunet, V., Jordan, P. & Cavalieri, A.V.G. 2017 Two-point coherence of wave packets in turbulent jets. *Phys. Rev. Fluids* **2** (2), 024604.

Jordan, P. & Colonius, T. 2013 Wave packets and turbulent jet noise. *Annu. Rev. Fluid Mech.* **45**, 173–195.

Karban, U., Martini, E. & Jordan, P. 2024 Modeling closed-loop control of installed jet noise using Ginzburg–Landau equation. *Flow Turbul. Combust.* **113** (3), 721–746.

KOPIEV, V., FARANOSOV, G., BYCHKOV, O., KOPIEV, V.A., MORALEV, I. & KAZANSKY, P. 2020 Active control of jet-plate interaction noise for excited jets by plasma actuators. *J. Sound Vib.* **484**, 115515.

KOPIEV, V.F., BELYAEV, I.V., ZAYTSEV, M.Y., KOPIEV, V.A. & FARANOSOV, G.A. 2013 Acoustic control of instability waves in a turbulent jet. *Acoust. Phys.* **59** (1), 16–26.

MAIA, I.A., JORDAN, P. & CAVALIERI, A.V.G. 2022 Wave cancellation in jets with laminar and turbulent boundary layers: the effect of nonlinearity. *Phys. Rev. Fluids* **7** (3), 033903.

MAIA, I.A., JORDAN, P., CAVALIERI, A.V.G., MARTINI, E., SASAKI, K. & SILVESTRE, F.J. 2021 Real-time reactive control of stochastic disturbances in forced turbulent jets. *Phys. Rev. Fluids* **6** (12), 123901.

MANCINELLI, M., JAUNET, V., JORDAN, P. & TOWNE, A. 2019 Screech-tone prediction using upstream-travelling jet modes. *Exp. Fluids* **60**, 1–9.

MANCINELLI, M., JORDAN, P. & LEBEDEV, A. 2024 Real-time estimation of jet-surface interaction noise. *Flow Turbul. Combust.* **113** (3), 579–599.

MANCINELLI, M., JORDAN, P., LEBEDEV, A. & KARI, R. 2022 Exploring flexible trailing edge properties to reduce installed jet noise in a jet-plate configuration. In *28th AIAA/CEAS Aeroacoustics 2022 Conference*, pp. 2872. AIAA Paper.

MARTINI, E., JUNG, J., CAVALIERI, A.V.G., JORDAN, P. & TOWNE, A. 2022 Resolvent-based tools for optimal estimation and control via the Wiener–Hopf formalism. *J. Fluid Mech.* **937**, A19.

NOBLE, B. & WEISS, G. 1959 Methods based on the Wiener–Hopf technique for the solution of partial differential equations. *Phys. Today* **12** (9), 50.

NOGUEIRA, P.A.S., CAVALIERI, A.V.G. & JORDAN, P. 2017 A model problem for sound radiation by an installed jet. *J. Sound Vib.* **391**, 95–115.

NOGUEIRA, P.A.S., SIROTTO, J.R.L.N., MIOTTO, R.F., CAVALIERI, A.V.G., CORDIOLI, J.A. & WOLF, W.R. 2019 Acoustic radiation of subsonic jets in the vicinity of an inclined flat plate. *J. Acoust. Soc. Am.* **146** (1), 50–59.

PIANTANIDA, S., JAUNET, V., HUBER, J., WOLF, W.R., JORDAN, P. & CAVALIERI, A.V.G. 2016 Scattering of turbulent-jet wavepackets by a swept trailing edge. *J. Acoust. Soc. Am.* **140** (6), 4350–4359.

PIERCE, A.D. 2019 *Acoustics: An Introduction to its Physical Principles and Applications*. Springer.

SANFILIPPO, D. & VALLE, A. 2013 Feedback systems: an analytical framework. *Comput. Music J.* **37** (2), 12–27.

SASAKI, K., MORRA, P., FABBIANE, N., CAVALIERI, A.V.G., HANIFI, A. & HENNINGSON, D.S. 2018*a* On the wave-cancelling nature of boundary layer flow control. *Theor. Comput. Fluid Dyn.* **32** (5), 593–616.

SASAKI, K., PIANTANIDA, S., CAVALIERI, A.V.G. & JORDAN, P. 2017 Real-time modelling of wavepackets in turbulent jets. *J. Fluid Mech.* **821**, 458–481.

SASAKI, K., TISSOT, G., CAVALIERI, A.V.G., SILVESTRE, F.J., JORDAN, P. & BIAU, D. 2018*b* Closed-loop control of a free shear flow: a framework using the parabolized stability equations. *Theor. Comput. Fluid Dyn.* **32** (6), 765–788.

SINHA, A., RODRÍGUEZ, D., BRÈS, G.A. & COLONIUS, T. 2014 Wavepacket models for supersonic jet noise. *J. Fluid Mech.* **742**, 71–95.

SIPP, D. & SCHMID, P.J. 2016 Linear closed-loop control of fluid instabilities and noise-induced perturbations: a review of approaches and tools. *Appl. Mech. Rev.* **68** (2), 020801.

WELCH, P. 1967 The use of fast Fourier transform for the estimation of power spectra: a method based on time averaging over short, modified periodograms. *IEEE Trans. Audio Electroacoust.* **15** (2), 70–73.